Supplementary Information

Carbon nanolayer-mounted single metal sites enable dipole polarization loss under electromagnetic field

Siyao Cheng,[†,1,2] Daohu Sheng,[†,3] Soumya Mukherjee,[4] Wei Dong,[3] Yuanbiao Huang,[2] Rong Cao,[2] Aming Xie[,1], Roland A. Fischer,[5] Weijin Li*[,6]*

Affiliations:

1. School of Safety Science and Engineering, Nanjing University of Science and Technology, Nanjing 210094, P. R. China.

2. State Key Laboratory of Structural Chemistry Fujian Institute of Research on the Structure of Matter, Chinese Academy of Sciences, Fuzhou 350002, P. R. China

3. School of Chemistry and Chemical Engineering, Nanjing University of Science and Technology, Nanjing 210094, P. R. China.

4. Bernal Institute, Department of Chemical Sciences, University of Limerick, Limerick V94 T9PX, Ireland.

5. Chair of Inorganic and Metal-Organic Chemistry, Department of Chemistry & School of Natural Sciences, Technical University of Munich, Lichtenbergstrasse 4, 85748, Garching, Germany.

6. School of Materials Science and Engineering, Nanjing University of Science and Technology, Nanjing 210094, P. R. China.

# These authors contribute equally.

* Correspondence: wjli@njust.edu.cn (Weijin Li); xieaming@njust.edu.cn (Aming Xie)

Contents

1. Supplementary Figures

The precursor $HMoO_3$@polypyrrole (HMO@PPy) was prepared according to our previous reported literature, followed by pyrolysis at 700°C to form HMO@Nitrogen-doped carbon (HMO@NC) (**Supplementary Fig. 1a**). As shown in **Supplementary Fig. 1b-e,** transmission electron microscopy (TEM) images of HMO@NC show that all of HMO@NC exhibit elongated nanorods with core-shell morphology and the carbon layer thickness thickens with increasing pyrrole ratio (mass ratios: HMO/pyrrole = 2:1; 1:1; 1:2). However, HMO@NC material has almost no EWM absorbing properties (**Supplementary Fig. 1f-1h**).

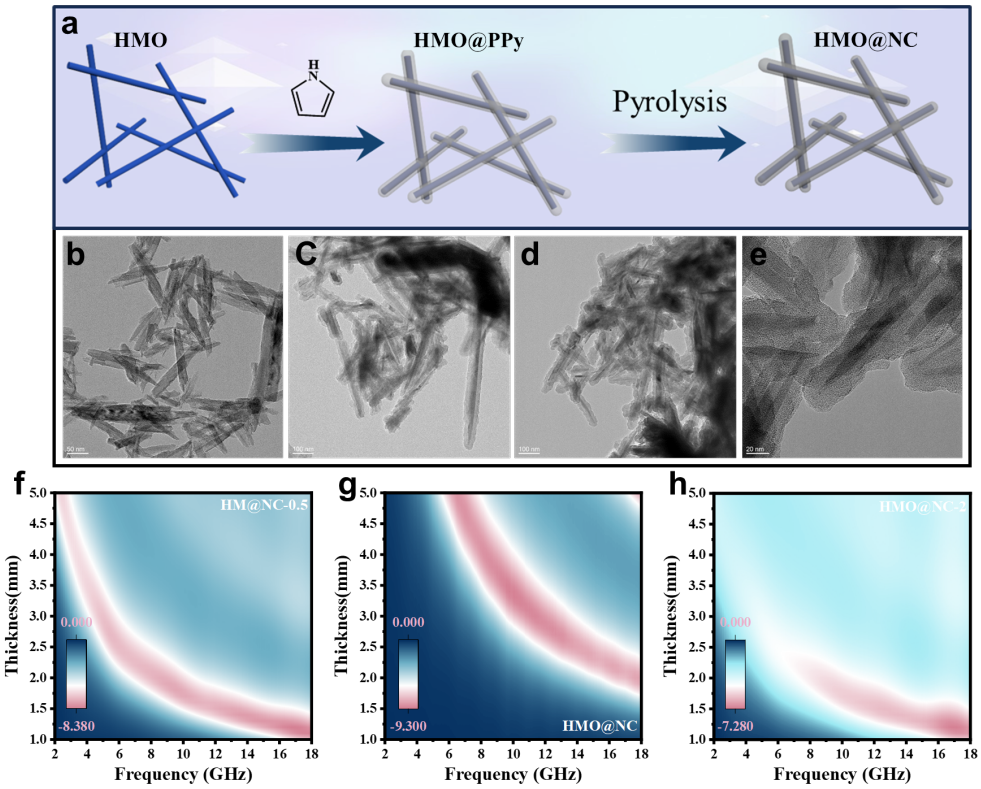

Supplementary Fig. 1 | HMO@NC preparation and characterization: a) Schematic diagram of the preparation of HMO@NC. TEM image of HMO@NC with different mass ratios of PPy: b) 2:1, c) 1:1 and c, d) 1:2. f) EWM absorption performance diagram of HMO@NC-0.5, g) HMO@NC and h) HMO@NC-2.

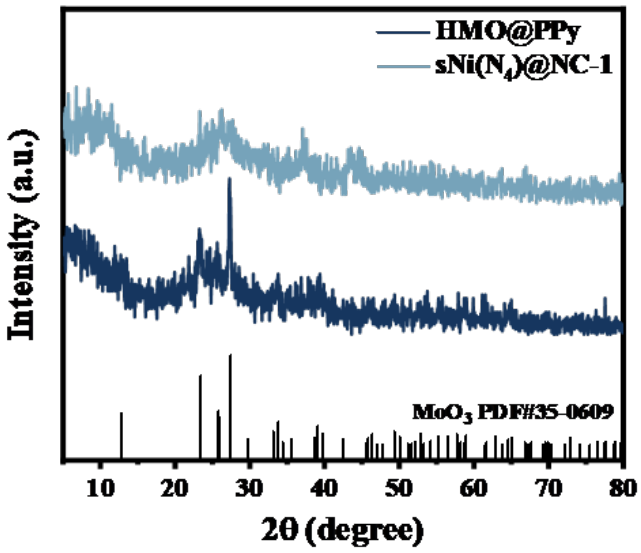

Supplementary Fig. 2 | X-ray diffraction (XRD) patterns of the samples.

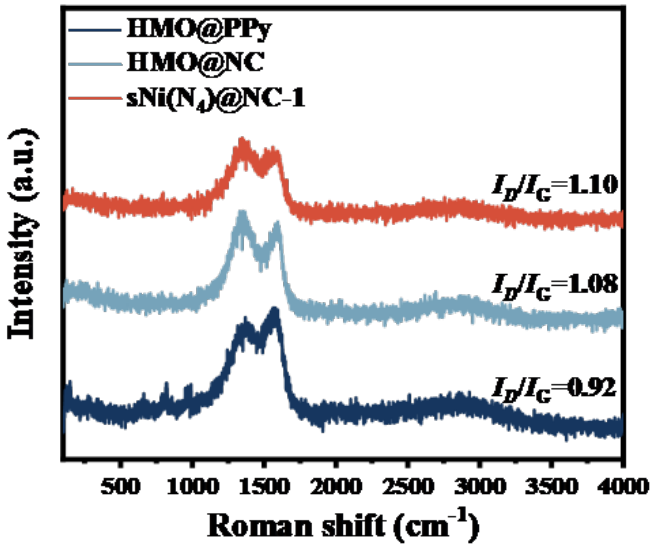

Supplementary Fig. 3 | Raman patterns of the samples.

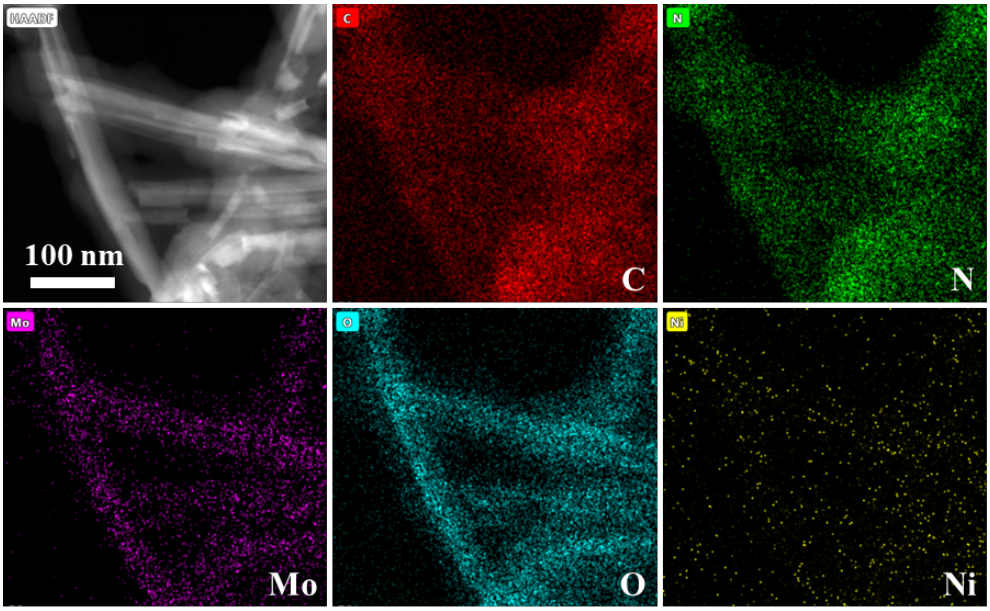

Supplementary Fig. 4 | EDS mapping images of sNi(N_4)@NC-1.

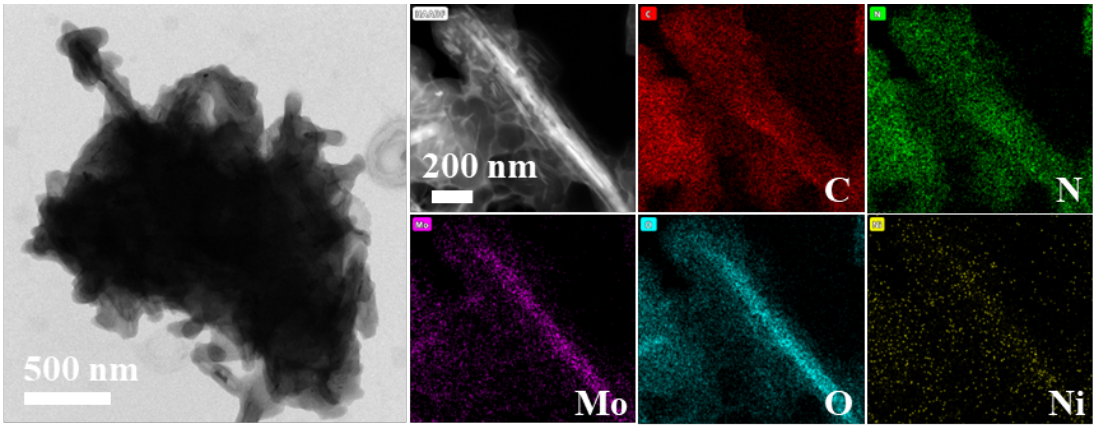

Supplementary Fig. 5 | HAADF-STEM and corresponding EDS mapping images of sNi(N_4)@NC-2.

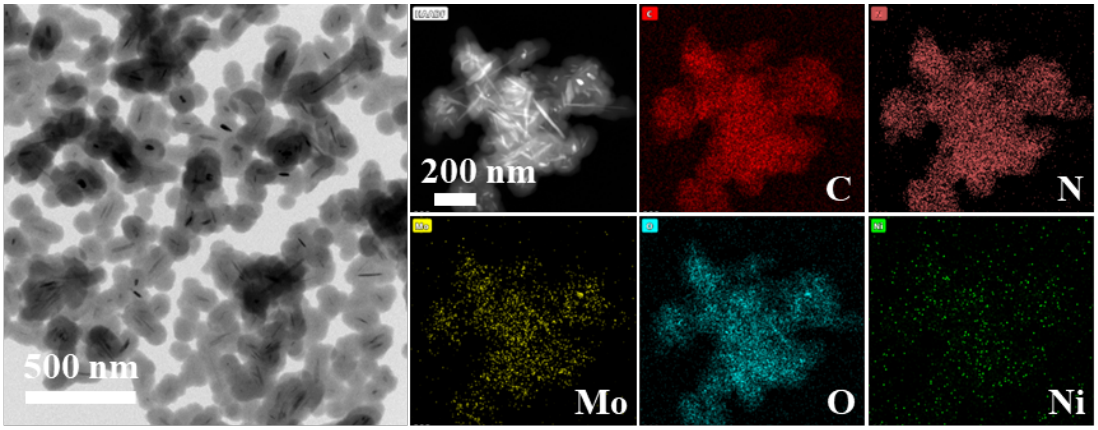

Supplementary Fig. 6 | HAADF-STEM and corresponding EDS mapping images of sNi(N_4)@NC.

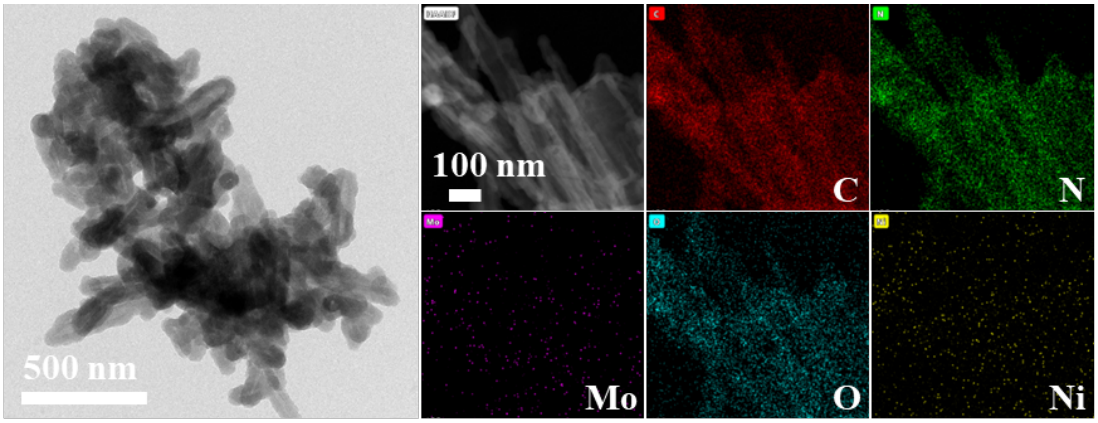

Supplementary Fig. 7 | HAADF-STEM and corresponding EDS mapping images of sNi(N_4)@NC-3.

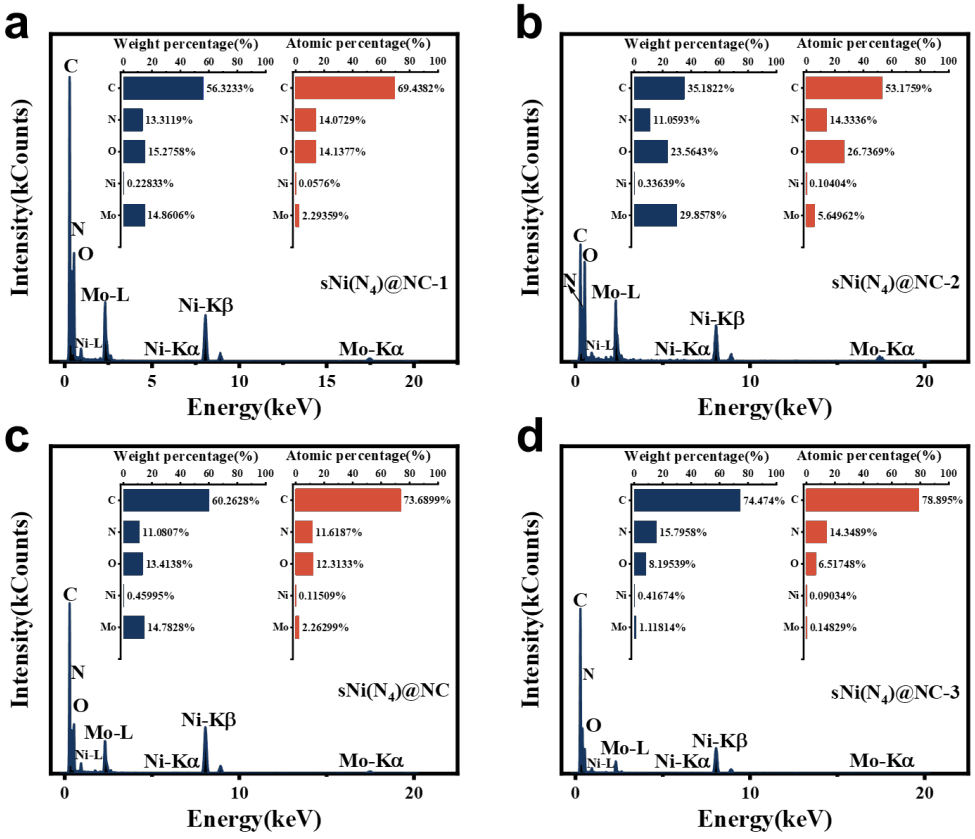

Supplementary Fig. 8 | EDX spectrum and corresponding element proportion statistics of a) sNi(N4)@NC-1, b) sNi(N4)@NC-2 c) sNi(N4)@NC and d) sNi(N4)@NC-3.

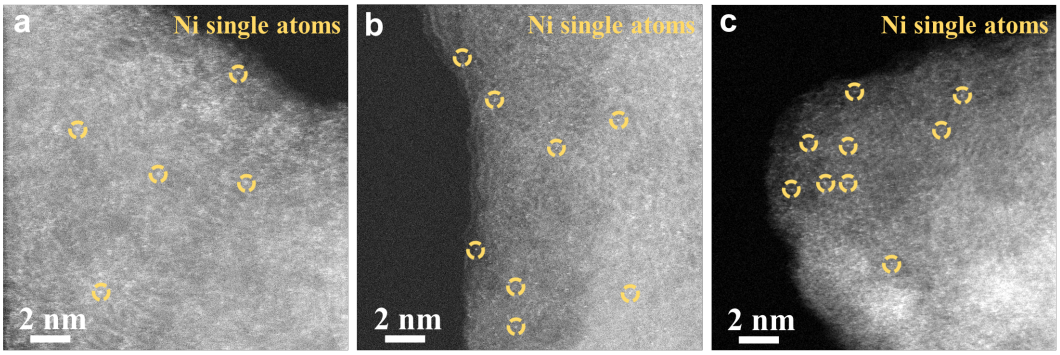

Supplementary Fig. 9 | Aberration-corrected high-angle annular dark-field scanning TEM images: a) sNi(N4)@NC-1, b) sNi(N4)@NC-2, c) sNi(N4)@NC.

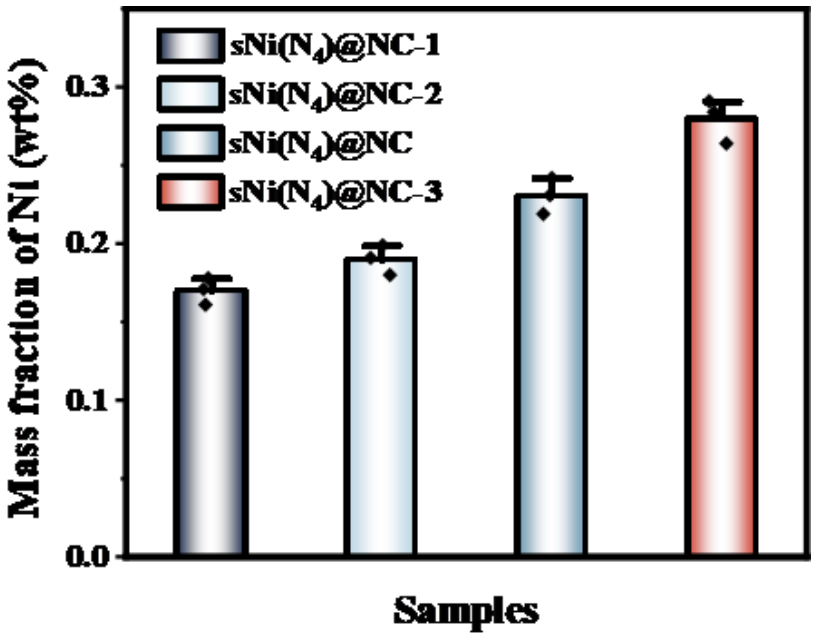

Supplementary Fig. 10 | ICP-OES spectrum of sNi(N_4)@NC-1, sNi(N_4)@NC-2, sNi(N_4)@NC and sNi(N_4)@NC-3. (Data are presented as mean ± SD (n = 3 independent samples)

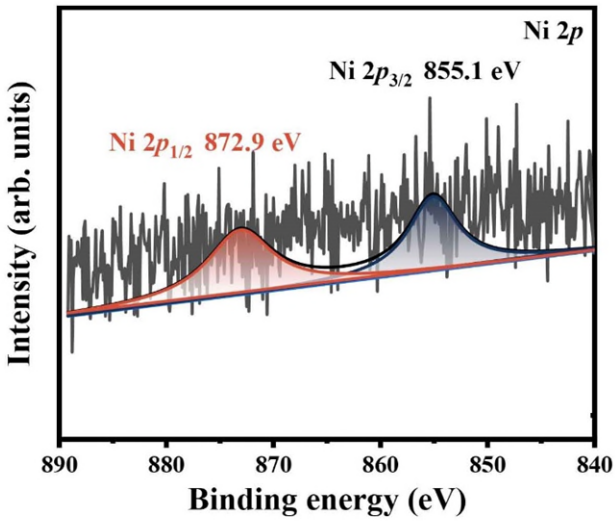

Supplementary Fig. 11 | Ni 2*p* XPS spectrum of sNi(N_4)@NC.

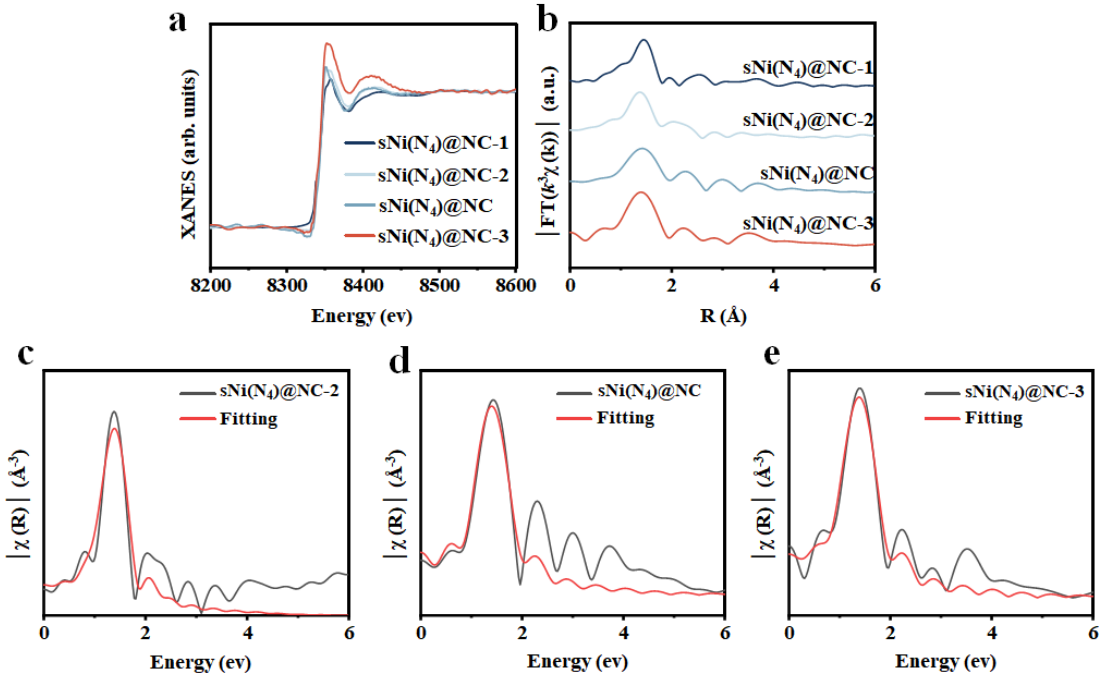

Supplementary Fig. 12 | a) XANES spectrum at the Ni K-edge, (b) EXAFS spectra in reciprocal space. EXAFS fitting results of c) sNi(N4)@NC-2, d) sNi(N4)@NC, and e) sNi(N4)@NC-3.

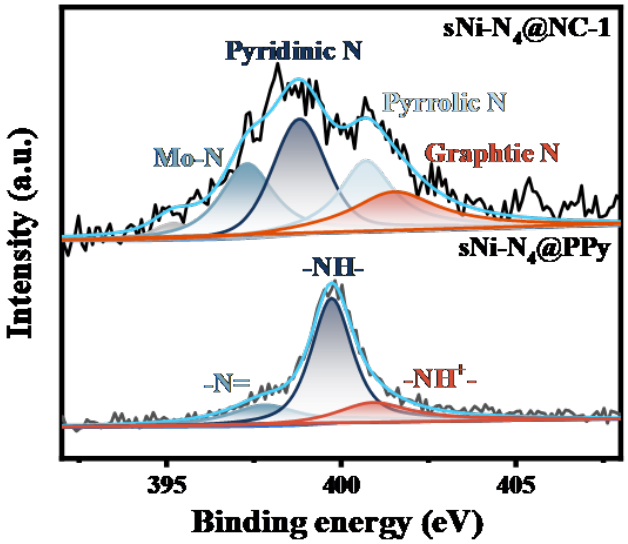

Supplementary Fig. 13 | N 1*s* XPS spectrum of sNi(N4)@NC-1 and sNi(N4)@PPy.

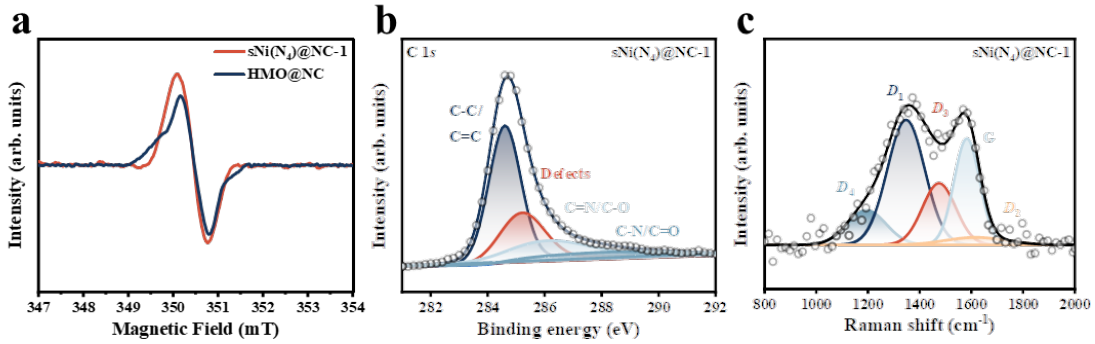

Supplementary Fig. 14 | Electron paramagnetic resonance and Ramman spectra measurement: a) EPR pattern of sNi(N_4)@NC-1 and HMO@NC. b) Deconvoluted C 1s spectra, c) Deconvoluted Raman spectra of sNi(N_4)@NC-1.

The C 1*s* spectra were deconvoluted into graphitic carbon (C−C) at 284.7 eV, defective carbon at 285.2 eV, C=N/C−O at 286.2 eV, and C−N/C=O at 289.3 eV. Raman peaks can be deconvoluted into five bands (polyenes at 1200 cm^{-1} for the D_4 band, graphene edges at 1350 cm^{-1} for the D_1 band, topological defects at 1500 cm^{-1} for the D_3 band, graphitic lattice at 1580 cm^{-1} for the G band, and surface graphene layers at 1620 cm^{-1} for the D_2 band).

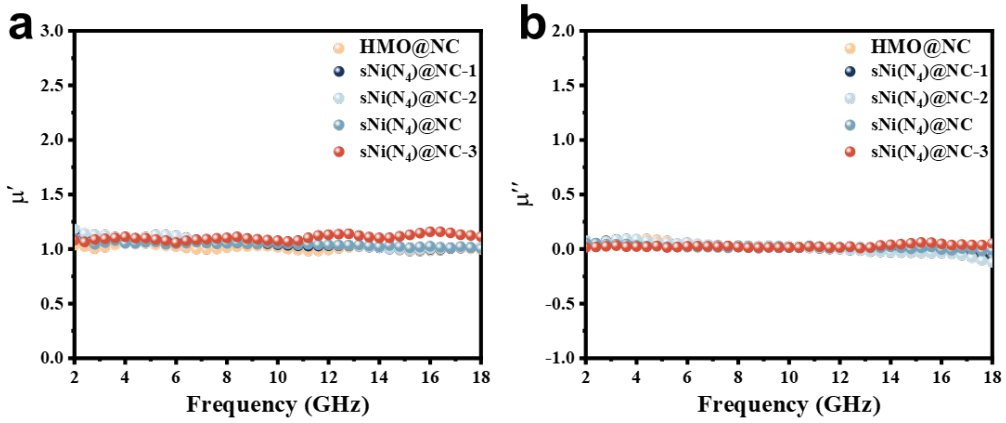

Supplementary Fig. 15 | a) Real and b) Imaginary part of permeability.

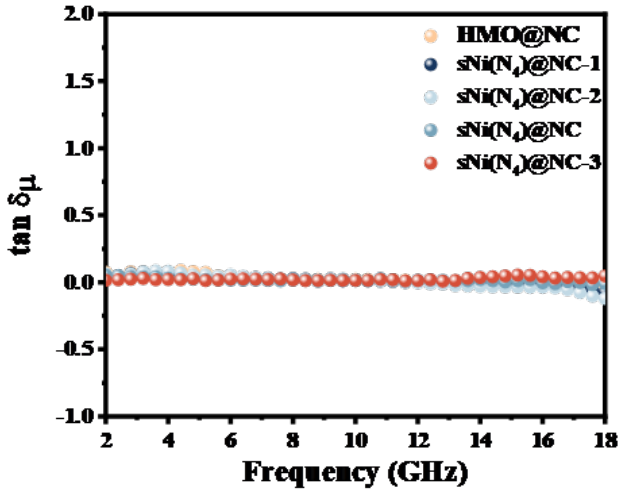

Supplementary Fig. 16 | Magnetic loss angular tangent of the samples.

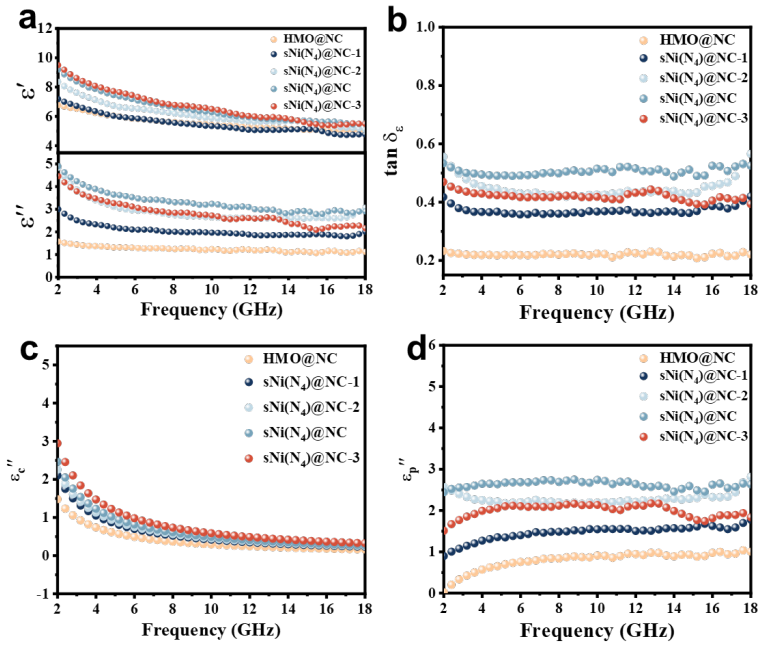

Supplementary Fig. 17 | Electromagnetic parameters tests**:** a) Real (ε′) and imaginary (ε″) part of permittivity, b) Tan δε, c) conduction loss (ε_c'') and d) Polarization relaxation loss (ε_p'') of HMO@NC, sNi(N_4)@NC-1, sNi(N_4)@NC-2, sNi(N_4)@NC and sNi(N_4)@NC-3.

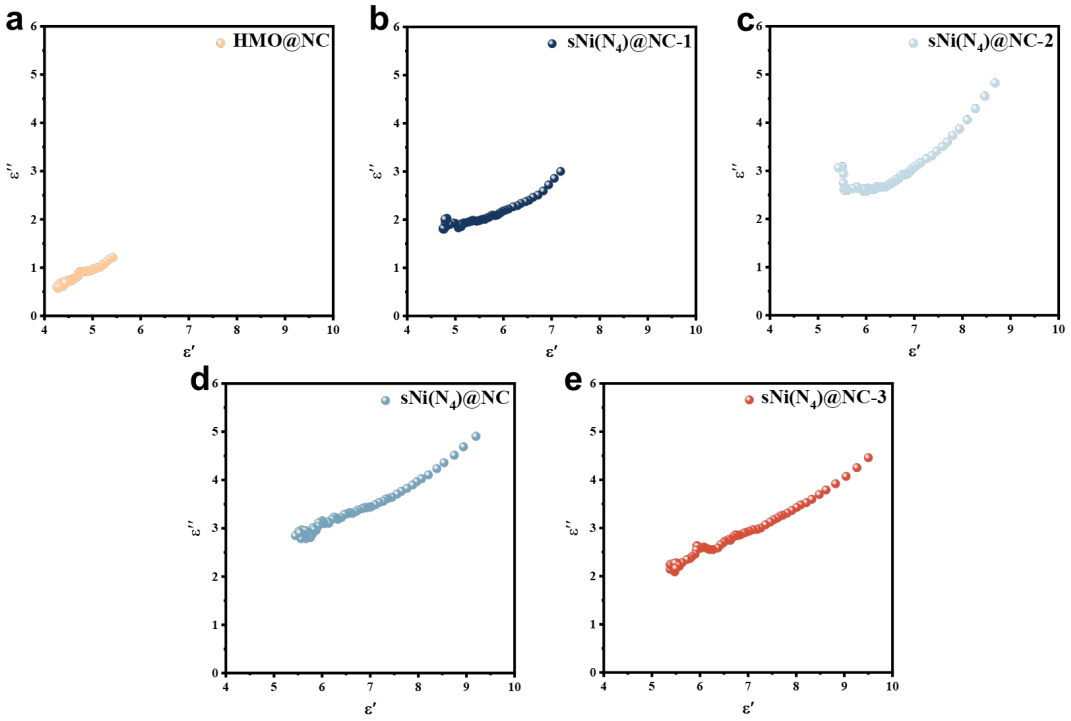

Supplementary Fig. 18 | Cole-Cole semicircles of a) HMO@NC, b) sNi(N4)@NC-1, c) sNi(N4)@NC-2, d) sNi(N4)@NC and e) sNi(N4)@NC-3.

Polarization relaxation is evaluated through Cole-Cole semicircles. Following Debye relaxation theory, the related equations of ε′ and ε″ are as follows: [1,2]

$$\varepsilon' = \varepsilon_\infty + \frac{\varepsilon_s - \varepsilon_\infty}{1 + \omega^2 \tau^2} \qquad (Equ.S1)$$

$$\varepsilon'' = \frac{\varepsilon_s - \varepsilon_\infty}{1 + \omega^2 \tau^2} + \frac{\sigma}{\omega \varepsilon_0} \qquad (Equ.S2)$$

$$(\varepsilon' - \frac{\varepsilon_s + \varepsilon_\infty}{2})^2 + (\varepsilon'')^2 = (\frac{\varepsilon_s - \varepsilon_\infty}{2})^2 \qquad (Equ.S3)$$

where ε_s, ε_∞, ω and τ are static permittivity, optical dielectric constant, angular frequency and polarization relaxation time, respectively. σ and ε_0 correspond to conductivity and the permittivity in a vacuum.

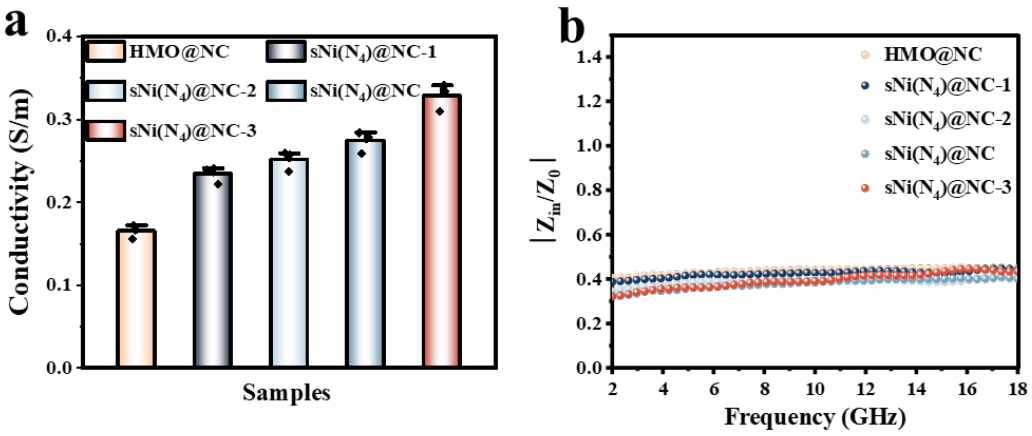

Supplementary Fig. 19 | a) Conductivity (Data are presented as mean ± SD (n = 3 independent samples) and b) Impedance matching of HMO@NC, sNi(N_4)@NC-1, sNi(N_4)@NC-2, sNi(N_4)@NC and sNi(N_4)@NC-3.

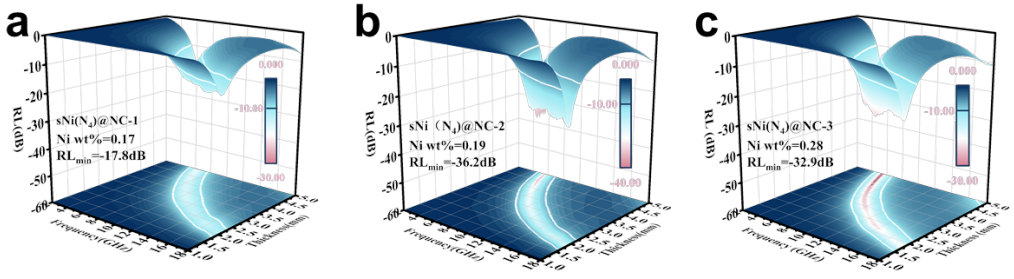

Supplementary Fig. 20 | 3D RL plots of a) sNi(N_4)@NC-1, b) sNi(N_4)@NC-2 and c) sNi(N_4)@NC-3.

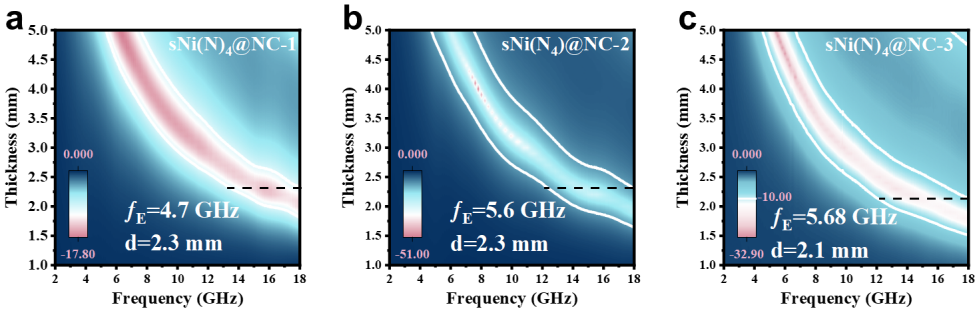

Supplementary Fig. 21 | 2D RL plots of a) sNi(N4)@NC-1, b) sNi(N4)@NC-2 and c) sNi(N4)@NC-3.

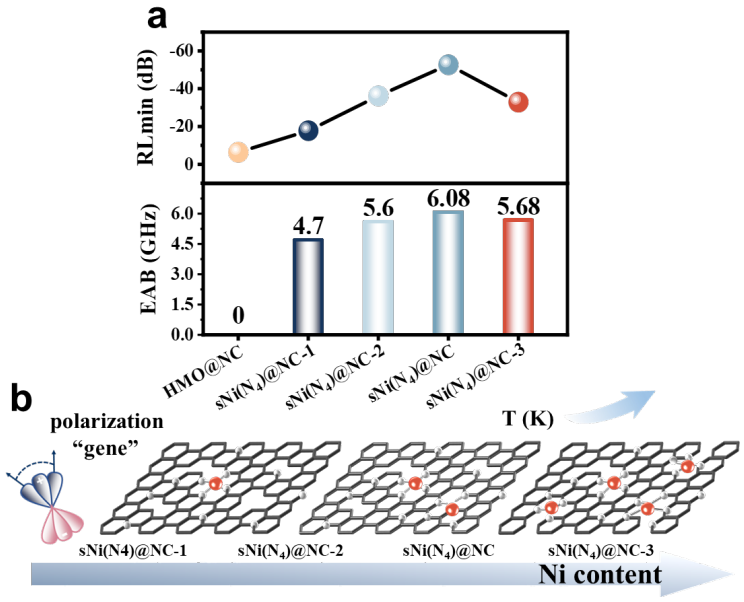

Supplementary Fig. 22 | a) Summary of EAB and RL_{min} for all the samples. b) As the reaction temperature increases, the content of Ni increases.

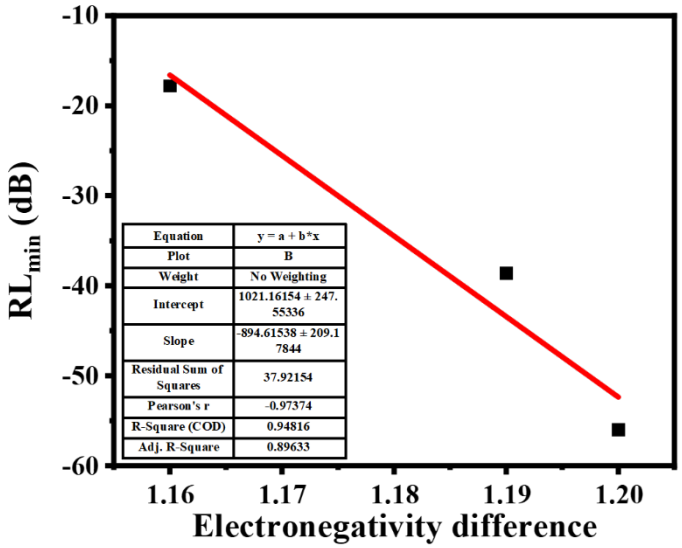

Supplementary Fig. 23 | Correlation analysis of between electronegativity difference and RL_{min}.

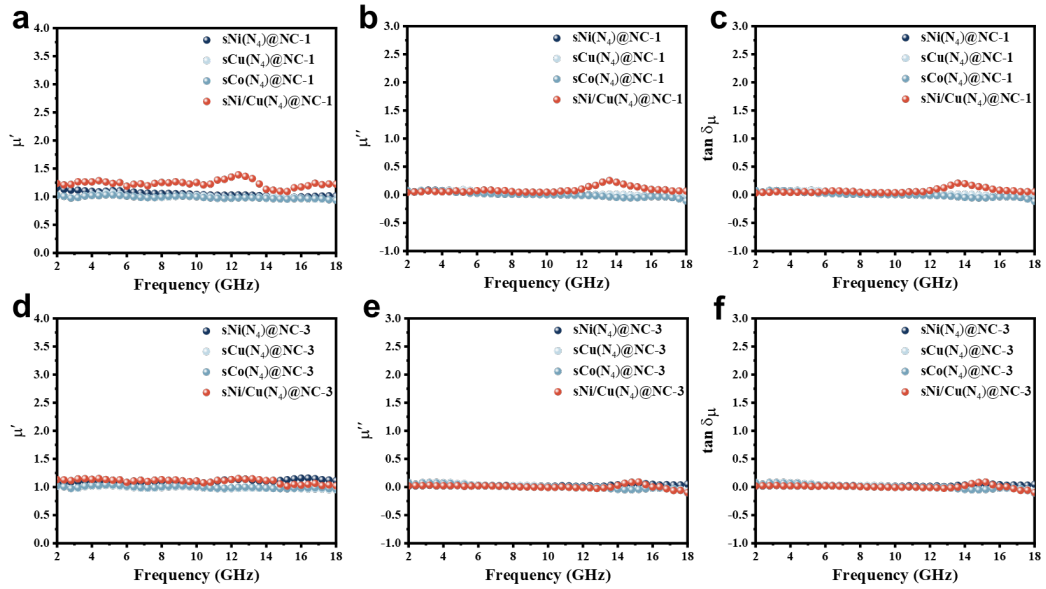

Supplementary Fig. 24 | Magnetic loss mechanism analysis. a) Real and b) Imaginary part of permeability, c) Tan δ_μ of sM(N_4)@NC-1 (M= Ni, Cu, Co and Ni/Cu). d) Real and e) Imaginary part of permeability, f) Tan δ_μ of sM(N_4)@NC-3 (M= Ni, Cu, Co and Ni/Cu).

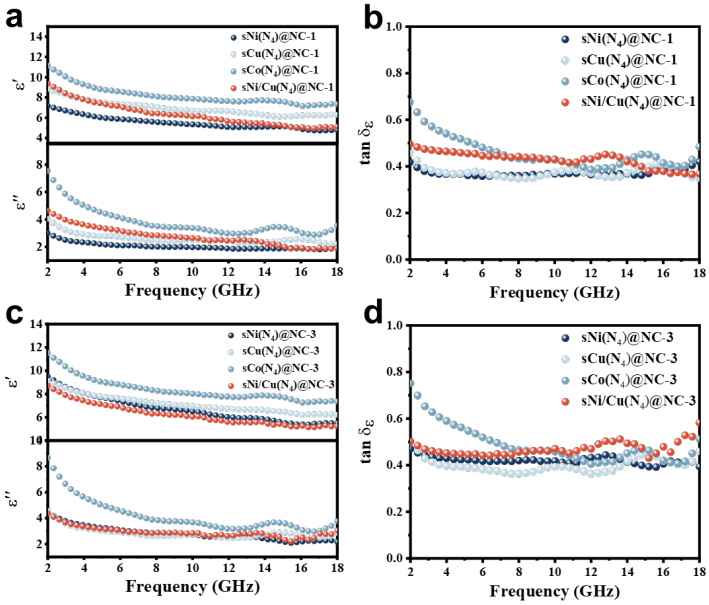

Supplementary Fig. 25 | Dielectric loss mechanism analysis. a) Real and imaginary part of permittivity, and b) Tan δ_ε of sM(N_4)@NC-1 (M= Ni, Cu, Co and Ni/Cu). c) Real and imaginary part of permittivity, and d) Tan δ_ε of sM(N_4)@NC-3 (M= Ni, Cu, Co and Ni/Cu).

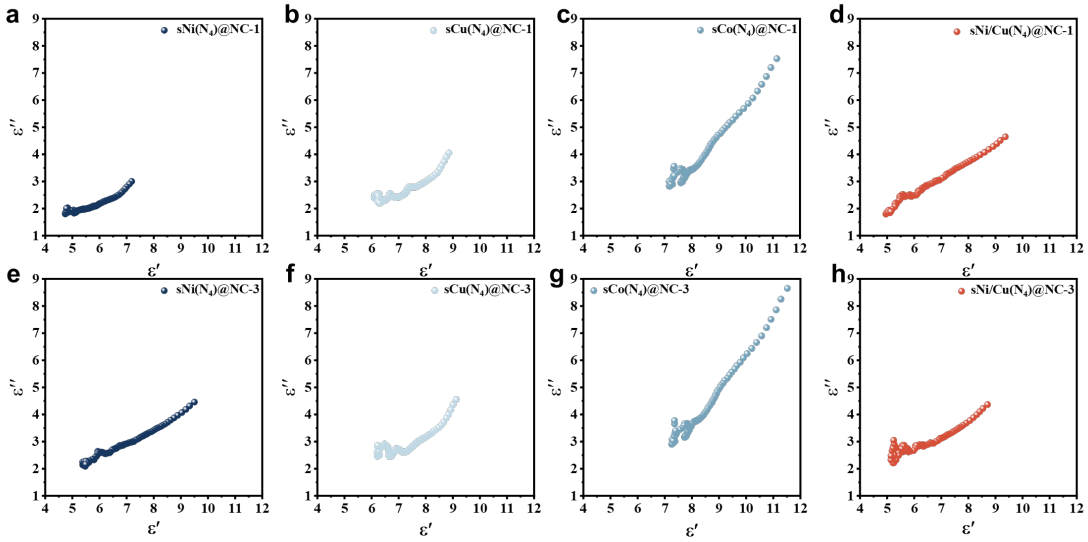

Supplementary Fig. 26 | Cole-Cole semicircles of a) sNi(N_4)@NC-1, b) sCu(N_4)@NC-1, c) sCo(N_4)@NC-1, d) sNi/Cu(N_4)@NC-1, e) sNi(N_4)@NC-3, f) sCu(N_4)@NC-3, g) sCo(N_4)@NC-3 and h) sNi/Cu(N_4)@NC-3.

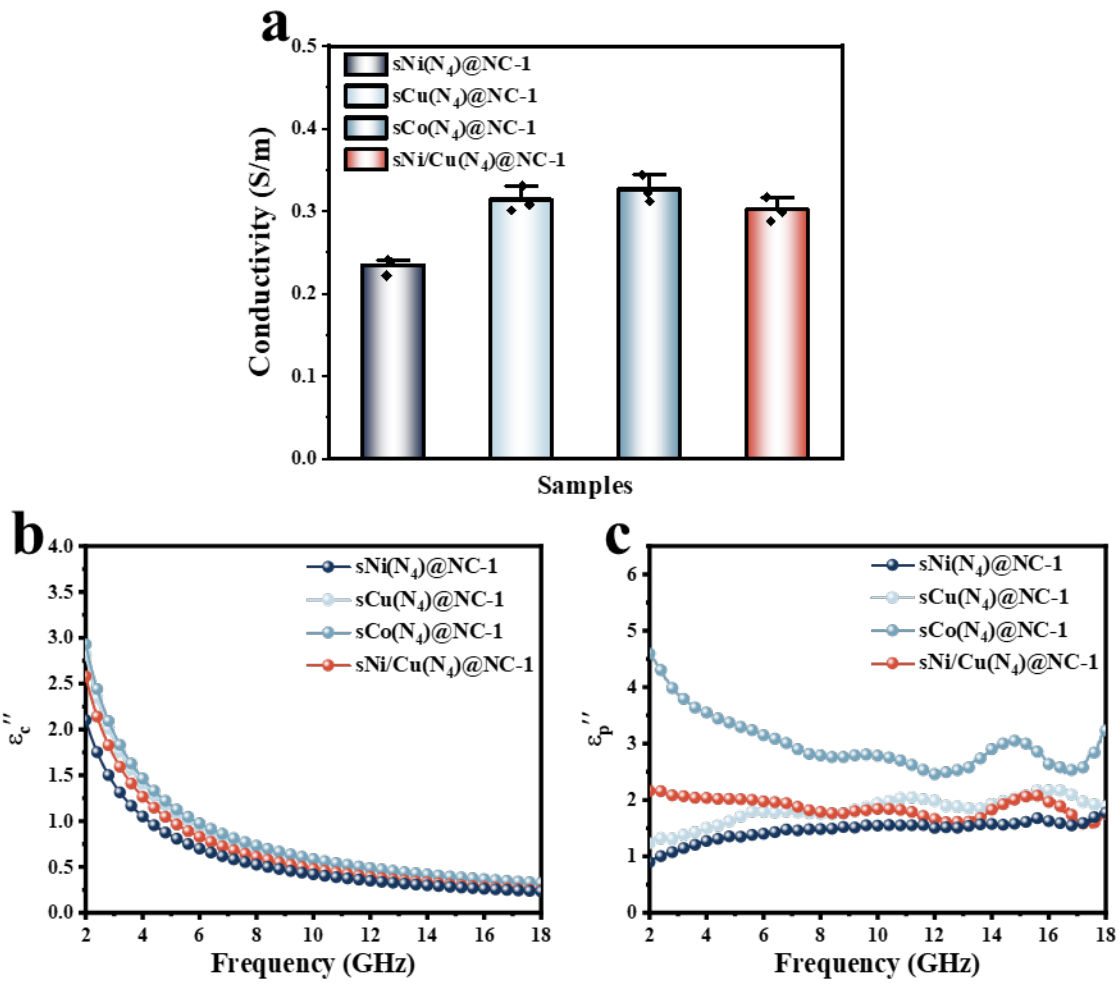

Supplementary Fig. 27 | a) Conductivity (Data are presented as mean ± SD (n = 3 independent samples), b) Conduction loss and c) Polarization relaxation loss of sM(N_4)@NC-1 (M= Ni, Cu, Co, Ni/Cu).

Since the material has no significant magnetization, the contribution of magnetic losses to the material is negligible (Supplementary Fig. 24). Among them, the minimum reflection loss of HMO@NC, sNi(N_4)@NC, sCu(N_4)@NC, sCo(N_4)@NC, and sNi/Cu(N_4)@NC is –9.3, –17.8, –38.6, –55.9, and –51.7 dB, respectively; the maximum absorption bandwidth is 0, 4.7, 4.6, 4.8, and 6.44, respectively. The results of the EWM absorbing properties are consistent with the pattern of their dielectric constant and dielectric loss curves (Supplementary Fig. 25). The sM(N_4)@NC and sM(N_4)@NC-3

materials exhibit multiple polarization relaxation processes (Supplementary Fig. 26). Polarization loss is stripped out by its conductive loss, it is found that sCo(N_4)@NC exhibits a higher polarization loss capacity, which aligns perfectly with its minimal reflection loss (Supplementary Fig. 27).

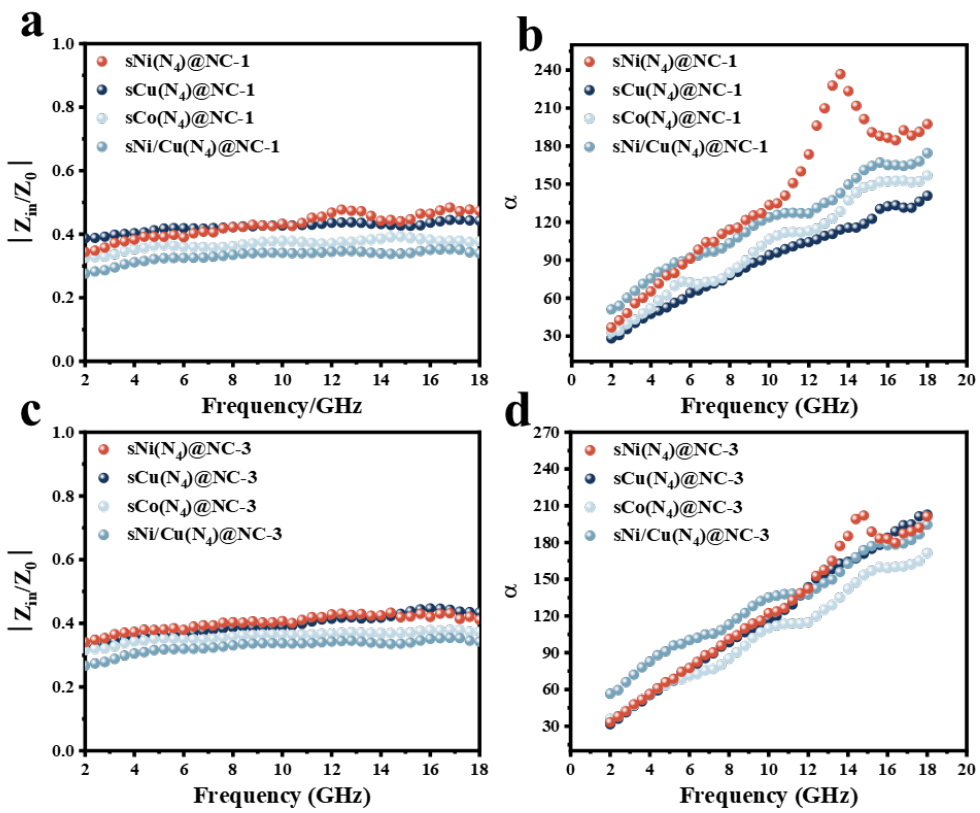

Supplementary Fig. 28 | a) Impedance matching and b) Attenuation constant of sM(N_4)@NC-1 (M= Ni, Cu, Co and Ni/Cu), c) Impedance matching and d) Attenuation constant of sM(N_4)@NC-3 (M= Ni, Cu, Co and Ni/Cu).

The attenuation ability can be revealed by the attenuation constant (α), which can be calculated via following equations: [3,4]

$$\alpha = \frac{\sqrt{2}\pi f}{c} \times \sqrt{(\mu''\varepsilon'' - \mu'\varepsilon') + \sqrt{(\mu''\varepsilon'' - \mu'\varepsilon')^2 + (\mu'\varepsilon'' - \mu''\varepsilon')^2}} \qquad (Equ. S4)$$

where Z_0 and Z_{in} embody the input impedance of the air and absorber, d is the thickness of absorber, f is the frequency of an electromagnetic wave and c represents the velocity of light in a vacuum.

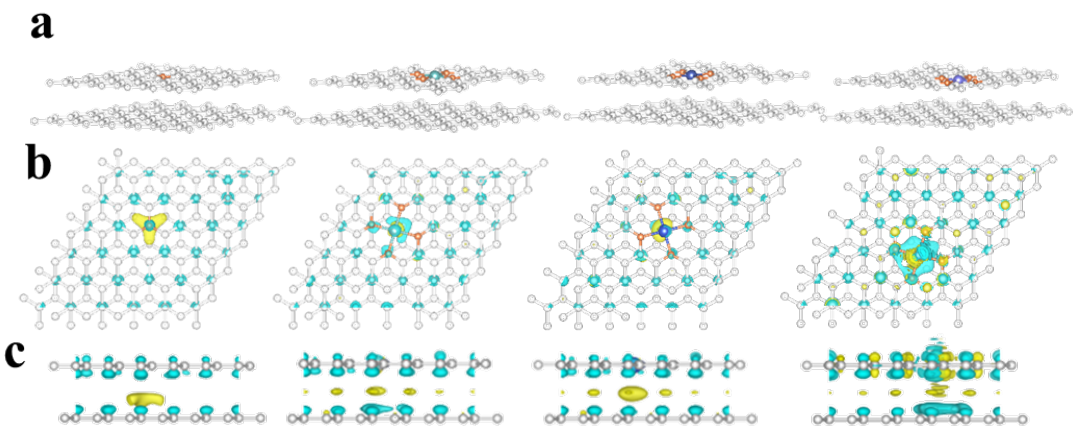

Supplementary Fig. 29 | Theoretical calculation: a) Atomic structure models and b, c) Differential charge density (From left to right, the order is HMO@NC, sNi(N_4)@NC-1, sCu(N_4)@NC-1 and sCo(N_4)@NC-1.

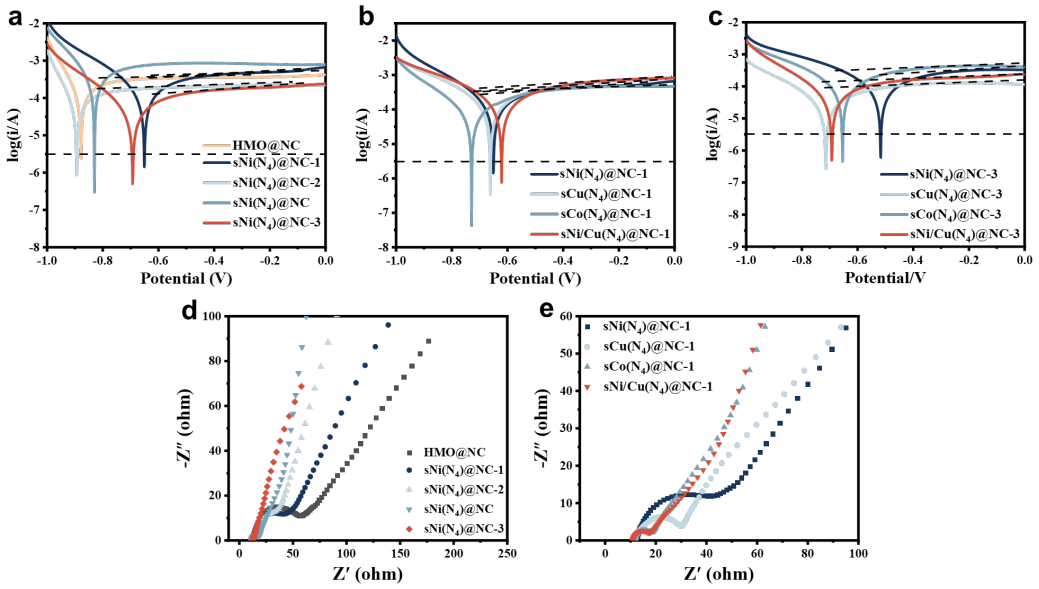

Supplementary Fig. 30 | a, b, c) Tafel plots of prepared samples and d, e) Electrochemical impedance spectra of prepared samples.

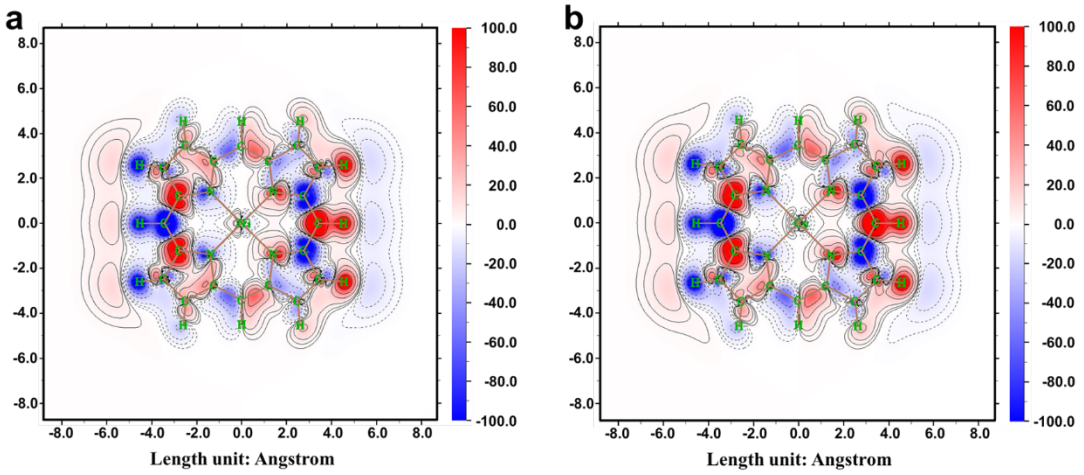

Supplementary Fig. 31 | Density of polarizability of a) sNi(N_4)@NC and b) sCu(N_4)@NC (The red and solid line parts represent areas where the electric field leads to an increase in density, while the blue and dashed lines correspond to areas where the density decreases).

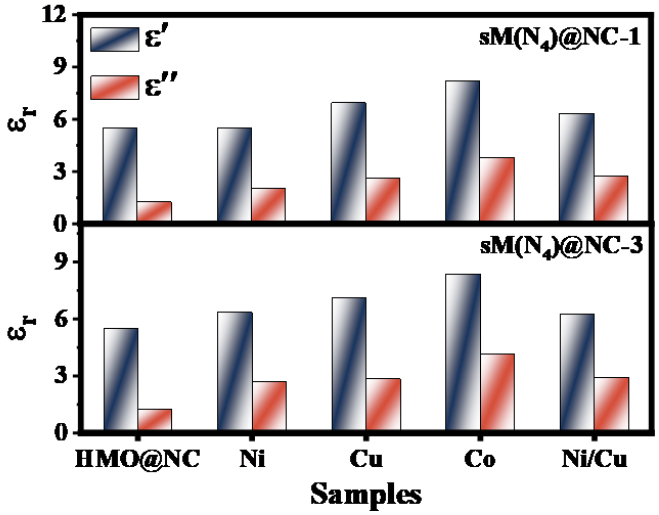

Supplementary Fig. 32 | The average value of ε' and ε″ of all samples**.**

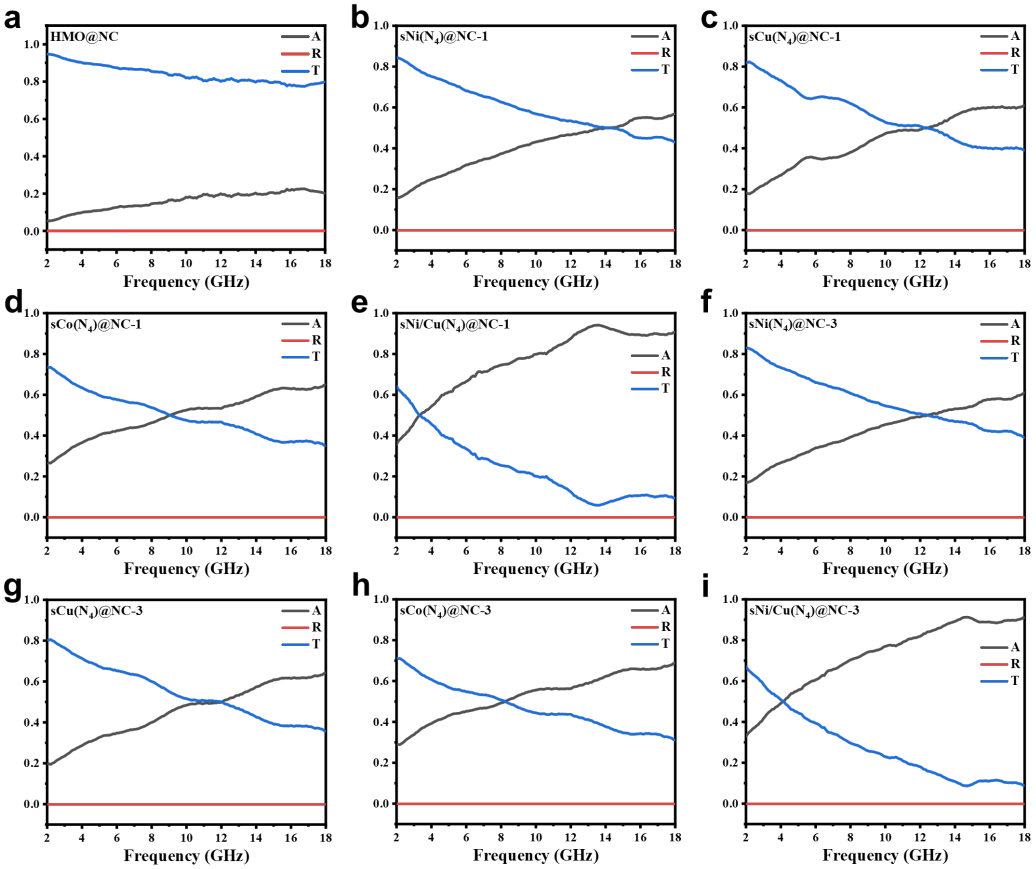

Supplementary Fig. 33 | The remaining energy after one-time EWM penetration. a-i) COMSOL Multiphysics simulation of all samples**.**

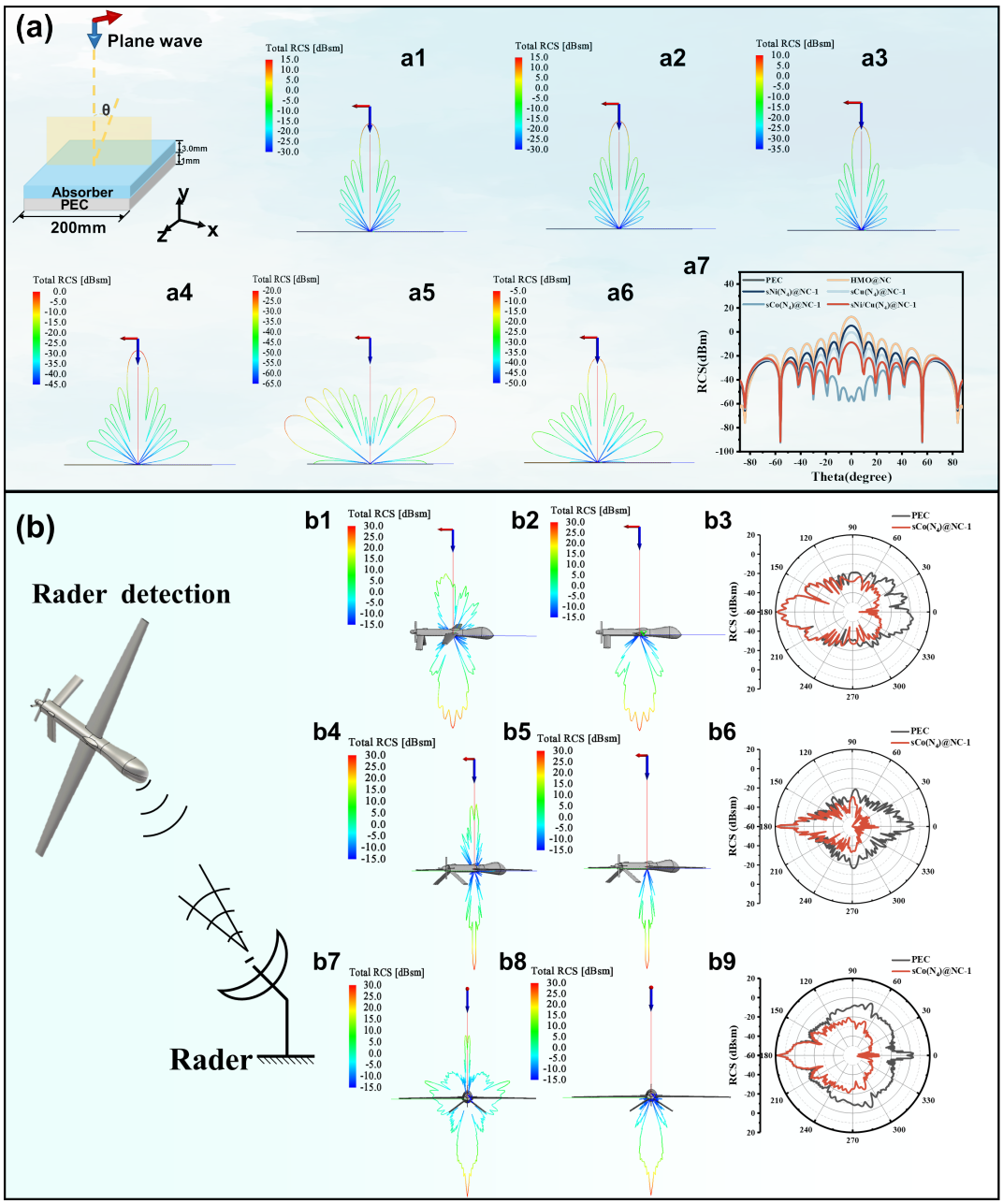

Supplementary Fig. 34 | Radar cross section (RCS) simulation by FEKO software. a) The sample coating thickness of 3 mm for metal back models and the monitor frequency was set as 9.04 GHz. Corresponding RCS simulation of a1) PEC, a2) HMO@NC, a3) sNi(N_4)@NC, a4) sCu(N_4)@NC, a5) sCo(N_4)@NC and a6) sNi/Cu(N_4)@NC, and a7) comparison of RCS simulation curves. b) The Predator 2 model simulated radar transmission angles of 0°, 45° and 90° at 9.04 GHz frequency, (b1, b4, b7) PEC; (b2, b5, b8) sCo(N_4)@NC; (b3, b6, b9) RCS polar summary diagram.

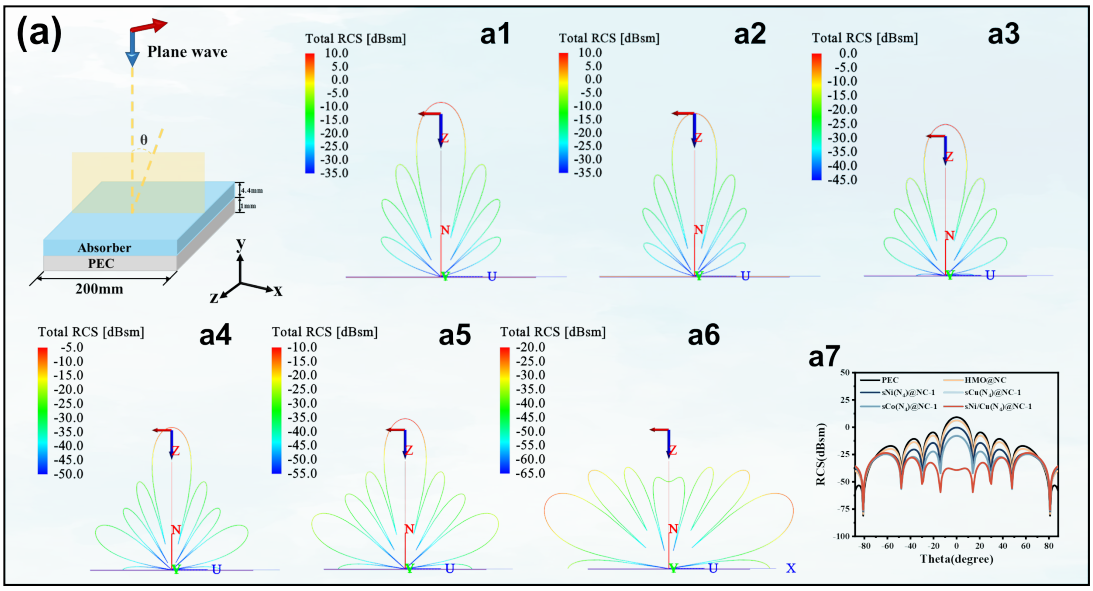

Supplementary Fig. 35 | RCS simulation: a) The sample coating thickness of 4.4 mm for metal back models and the monitor frequency was set as 6.08 GHz. Corresponding RCS simulation of a1) PEC, a2) HMO@NC, a3) sNi(N_4)@NC, a4) sCu(N_4)@NC, a5) sCo(N_4)@NC and a6) sNi/Cu(N_4)@NC, and a7) comparison of RCS simulation curves.

To verify the effective enhancement of EMW absorption performance of sM(N_4)@NC by surface modification of sM(N_4), the radar cross section (RCS) simulation was performed using FEKO software. The metal back (PEC) (Supplementary Fig. 34a) and Predator 2 (Supplementary Fig. 34b) were selected as the simulation model. First, the metal-back simulation model consists of a bottom PEC

plate (200 mm x 200 mm x 1 mm) and an upper coating (HMO@NC and sM(N_4)@NC-1, 3.00 mm), and the RCS signals of different surface coatings are obtained through the FEKO software (Supplementary Fig. 34a1-34a6). From the summarized 2D plot (Supplementary Fig. 34a7 and Supplementary Table 10), it can be clearly seen that the RCS values of the samples at 0° are ranked from high to low as follows: PEC (12.62 dBsm) > HMO@NC (12.62 dBsm) > sNi(N_4)@NC-1 (5.28 dBsm) > sCu(N_4)@NC-1 (-0.23 dBsm) > sNi/Cu(N_4)@NC-1 (-8.69 dBsm) > sCo(N_4)@NC-1 (-53.61 dBsm). This indicates that surface modification of sNi(N_4) can significantly enhance the electromagnetic loss capability of HMO@NC on metal backplates. In addition, we can modulate the RCS value of the sample at 0° by adjusting the coating thickness (Supplementary Fig. 35). To comprehensively evaluate the application potential of sCo(N_4)@NC-1 in real-world scenarios, we employed the Predator 2 model to simulate radar transmission angles of 0°, 45°, and 90° at a frequency of 9.04 GHz. In this way, we can more accurately predict the material's performance in actual applications and provide strong support for further applied research. From Supplementary Fig. 34b1-34b3, When the radar transmission angle is 0°, there is almost no radar scattering signal on the upper layer of the aircraft, and the ΔRCS value can reach -49.59 dBsm (Supplementary Table 11). When the transmission angle is adjusted to 45° and 90°, the radar scattering signal range on the aircraft surface changes significantly compared to 0°. After coating with sCo(N_4)@NC-1, the radar scattering signal on the upper layer of the aircraft also significantly weakens (Supplementary Fig. 34b4-34b9). The results show that the Predator 2 coated with sCo(N_4)@NC-1 exhibits excellent RCS attenuation capability regardless of incidence angle.

3. Supplementary Tables

Supplementary Table 1 | The content of Ni in different samples measured by ICP-OES**.**

Sample	The metal content of Ni (wt%)
sNi(N_4)@NC-1	0.17
sNi(N_4)@NC-2	0.19
sNi(N_4)@NC	0.23
sNi(N_4)@NC-3	0.28

Supplementary Table 2 | Parameters of the Ni K-edge EXAFS fitting results for sample**.**

Sample	shell	CN	R (Å)	ΔE_0(eV)	$\sigma^2\times10^3$(Å^2)	R-factor
SNi(N_4)@NC-1	Ni-N	3.9	1.87	0.70	3.533	0.022
SNi(N_4)@NC-2	Ni-N	3.6	1.86	2.67	12.6	0.032
SNi(N_4)@NC	Ni-N	3.7	1.91	4.80	15.6	0.026
SNi(N_4)@NC-3	Ni-N	4.0	1.89	5.25	-18.3	0.008

CN, coordination number; R, distance between absorber and backscatter atoms; ΔE_0, the inner potential correction; σ^2, Debye–Waller factor to describe the variance due to disorder (both lattice and thermal); R-factor is used to evaluate the quality of the fitting and the smaller value means more satisfied fitting; Fitting R-range=1-2.3; Fitting k-range=3-11.2.

Supplementary Table 3 | Fitting data of N 1s Spectrum.

N1s	Binding energy (eV)	Area ratio (%)
Pyridinic N	398.8	32.4
Pyrrolic N	400.7	23.8
Graphtie N	401.5	19.7
Mo-N	397.3	24.1

Supplementary Table 4 | Comparison of EMW absorption performance of sNi(N_4)@NC and sNi(N_4)@NC-X (X= 1, 2, 3) samples prepared at different temperatures.

Absorbers	Thickness (mm)	EAB (GHz)	RL_{min} (dB)
sNi(N_4)@NC-1	2.3	4.7	-17.8
sNi(N_4)@NC-2	2.3	5.6	-36.2
sNi(N_4)@NC	2.3	6.08	-52.7
sNi(N_4)@NC-3	2.3	5.68	-32.9

Supplementary Table 5 | Comparison of EMW absorption performance of the different sM(N_4) samples**.**

Absorbers	Thickness (mm)	EAB (GHz)	RL_{min} (dB)
sNi(N_4)@NC-1	2.3	4.7	-17.8
sCu(N_4)@NC-1	2.1	4.6	-38.6
sCo(N_4)@NC-1	2.0	4.8	-55.9
sNi/Cu(N_4)@NC-1	2.1	6.44	-51.8
sNi(N_4)@NC-3	2.3	5.68	-32.9
sCu(N_4)@NC-3	2.1	5.1	-34.1
sCo(N_4)@NC-3	2.0	5.0	-49.8
sNi/Cu(N_4)@NC-3	2.3	6.2	-45.4

Supplementary Table 6 | Comparison of EMW absorption performance of some representative carbon-based absorbers**.**

Absorbers	Thickness (mm)	EAB (GHz)	RL_{min} (dB)	Ref
$CoMoO_4$@C	5.0	3.45	-26.0	[5]
C@$NiCo_2O_4$@ Fe_3O_4	3.4	2.10	-43.0	[6]
Fe_3O_4@PANI	2.0	3.75	-23.7	[7]
Co-C/MWCNTS	2.5	3.60	-50.0	[8]
C@$NiCo_2O_4$	1.5	4.16	-39.0	[9]

Fe_3O_4@C	4.0	5.80	-43.5	[10]
sCo(N_4)@NC-1	2.0	4.80	-55.9	This work
sNi/Cu(N_4)@NC-1	2.1	6.44	-51.7	This work

Supplementary Table 7 | Mulliken charge (local of NC and MN4 structure) for all the samples**.**

	NC	**Ni**	**Cu**	**Co**
C	0.370	0.0252	0.234	0.243
N	-0.370	-0.321	-0.424	-0.551
MN_4		0.070	0.190	0.307

Supplementary Table 8 | The dipole moment calculations of HMO@NC, sNi(N_4)@NC, sCu(N_4)@NC and sCo(N_4)@NC, and their corresponding values to the μ (x, y, z) component of the dipole vector. μ is the magnitude of each vector. All values are in units of Debye.

Sample	μ_x	μ_y	μ_z	μ
HMO@NC	1.4505	2.2213	-0.0234	2.6529
sNi(N_4)@NC	0.9850	1.1210	-0.02442	1.4925
sCu(N_4)@NC	1.3299	1.7386	0.000556	2.1890
sCo(N_4)@NC	1.7613	2.4557	0.01403	3.0220

Supplementary Table 9 | The RCS values at θ = 0°**.**

	RCS value (dBsm)
PEC	12.627
HMO@NC	12.623
sNi(N_4)@NC-1	5.285
sCu(N_4)@NC-1	-0.236
sCo(N_4)@NC-1	-53.618
sNi/Cu(N_4)@NC-1	-8.695

Supplementary Table 10 | The average ΔRCS of different detection angles.

detection angle	**ΔRCS (dBsm)**
0°	-8.01
45°	-14.96
90°	-15.25

Supplementary Table 11 | Electromagnetic parameters and physical significance.

Electromagnetic parameter	Physical significance
ε_r	Complex permittivity (the material's ability to respond to an electric field)
μ_r	Complex permeability (the materials' response to a magnetic field)
ε' and μ'	Real part (the ability to store energy)
ε'' and μ''	imaginary part (the ability to lose energy)
Z_{in}	impedance of absorbers
Z_0	impedance of free-space
f	incident EMW frequency
d	thickness of absorbers
c	velocity of light
ε_s	static permittivity
ε_∞	optical dielectric constant
ω	angular frequency
τ	polarization relaxation time
α	attenuation constant

Supplementary Table 12 | ε′, ε″, ε_c, ε_p average values of HMO@NC, sNi(N_4)@NC, sNi(N_4)@NC-1, sNi(N_4)@NC-2 and sNi(N_4)@NC-3.

	ε'_{av}	ε''_{av}	$\varepsilon_{c,\,av}$	$\varepsilon_{p,\,av}$
HMO@NC	5.47	1.24	0.41	0.81
sNi(N_4)@NC	5.52	2.05	0.58	1.47
sNi(N_4)@NC-1	6.46	2.90	0.62	2.28
sNi(N_4)@NC-2	6.55	3.31	0.68	2.63
sNi(N_4)@NC-3	6.67	2.81	0.81	2.0

Supplementary Table 13 | ε′, ε″, ε_c, ε_p average values of HMO@NC, sNi(N_4)@NC, sCu(N_4)@NC, sCo(N_4)@NC and sNi/Cu(N_4)@NC.

	ε'_{av}	ε''_{av}	$\varepsilon_{c,\,av}$	$\varepsilon_{p,\,av}$
HMO@NC	5.47	1.24	0.41	0.81
sNi(N_4)@NC	5.52	2.05	0.58	1.47
sCu(N_4)@NC	6.94	2.60	0.77	1.82
sCo(N_4)@NC	8.19	3.80	0.81	3.0
sNi/Cu(N_4)@NC	6.33	2.75	0.72	1.87

Supplementary Table 14 | ε′, ε″ average values of HMO@NC, sNi(N_4)@NC-3, sCu(N_4)@NC-3, sCo(N_4)@NC-3 and sNi/Cu(N_4)@NC-3.

	ε'_{av}	ε''_{av}
HMO@NC	5.47	1.24
sNi(N_4)@NC-3	6.35	2.71
sCu(N_4)@NC-3	7.13	2.84
sCo(N_4)@NC-3	8.36	4.15
sNi/Cu(N_4)@NC-3	6.22	2.91

4. Supplementary References

1. Li, B. et al. Graphene-assisted assembly of electrically and magnetically conductive ceramic nanofibrous aerogels enable multifunctionality. *Adv. Funct. Mater.* **34**, 2314653 (2024).
2. Cao, M. et al. Thermally driven transport and relaxation switching self-powered electromagnetic energy conversion. *Small* **14**, 1800987 (2018).
3. Liang, L. et al. Multifunctional magnetic $Ti_3C_2T_x$ MXene/graphene aerogel with superior electromagnetic wave absorption performance. *ACS Nano* **15**, 6622 (2021).
4. Wu, C. et al. Hollow gradient-structured iron-anchored carbon nanospheres for enhanced electromagnetic wave absorption. *Nano-Micro Lett.* **15**, 7 (2023).
5. Xie, A. et al. Enhancing electromagnetic absorption performance of Molybdate@Carbon by metal ion substitution. *J. Mater. Sci. Technol.* **163**, 92 (2023).
6. Wei, S. et al. Preparation of hierarchical core-shell C@$NiCo_2O_4$@Fe_3O_4 composites for enhanced microwave absorption performance. *Chem. Eng. J.* **314**, 477 (2017).

7. Yang, W. et al. Construction and microwave absorption properties of core@double-shell structured Fe_3O_4@polyaniline@MnO_2 Nanospheres. *Nano* **15**, 2050032 (2020).
8. Shu, R. et al. Nitrogen-doped Co-C/MWCNTs nanocomposites derived from bimetallic metal–organic frameworks for electromagnetic wave absorption in the X-band. *Chem. Eng. J.* **362**, 513 (2019).
9. Li, C. et al. The rambutan-like C@$NiCo_2O_4$ composites for enhanced microwave absorption performance. *J. Mater. Sci.: Mater. Electron.* **30**, 3124 (2019).
10. Fu, C. et al. Enhanced microwave absorption properties of polyaniline-modified porous Fe_3O_4@C nanosheets. *J. Mater. Sci.: Mater. Electron.* **30**, 11907 (2019).